https://doi.org/10.1016/j.electacta.2021.137967

Investigation on the electrochemical performance of hybrid zinc batteries through numerical analysis

Yanyi Ma[a], Wentao Yu[a], Wenxu Shang[a], Xu Xiao[a], Yawen Dai[b], Chun Cheng[b], Meng Ni[bc], Peng Tan[a]

a Department of Thermal Science and Energy Engineering, University of Science and Technology of China, Hefei 230026, Anhui, China
b Department of Building and Real Estate, The Hong Kong Polytechnic University, Hung Hom, Kowloon, Hong Kong, China
c Environmental Energy Research Group, Research Institute for Sustainable Urban Development (RISUD), The Hong Kong Polytechnic University, Hung Hom, Kowloon, Hong Kong, China

Highlights

- A mathematical model of a hybrid Zn–Co/air battery is first developed.
- The effects of discharge depth, reaction interface, and degradation are studied.
- The work guides the design of interfaces and the selection of operating conditions.

Abstract

With the rapid expansion of the electric vehicle market, the demand for advanced energy storage technologies is increasing strongly. An alkaline hybrid zinc battery with cobalt oxide as the positive electrode material combines the advantages of the high working voltage of Zn–Co batteries and the excellent discharge capacity of Zn–air batteries simultaneously. However, the development of hybrid zinc batteries is limited by their low energy efficiency and poor cycling stability. To investigate the charge–discharge behaviors of hybrid zinc batteries, a mathematical model is established, coupling the mass transport inside the porous electrode with energy conversion. Then, the effects of discharge depth, reaction interfaces, and active material degradation on energy efficiency are investigated through numerical analysis. It is found that within a proper region, the higher ratio of two-phase and three-phase interfaces can lead to higher energy efficiency, and the increase of the two-phase interfaces is beneficial for improving energy

efficiency. While the effects of active material degradation on energy efficiency are significant, resulting in poor cycling stability. This work is favorable for the design of interfaces and the selection of operating conditions, and guides the performance improvement of hybrid zinc batteries.

Graphical abstract

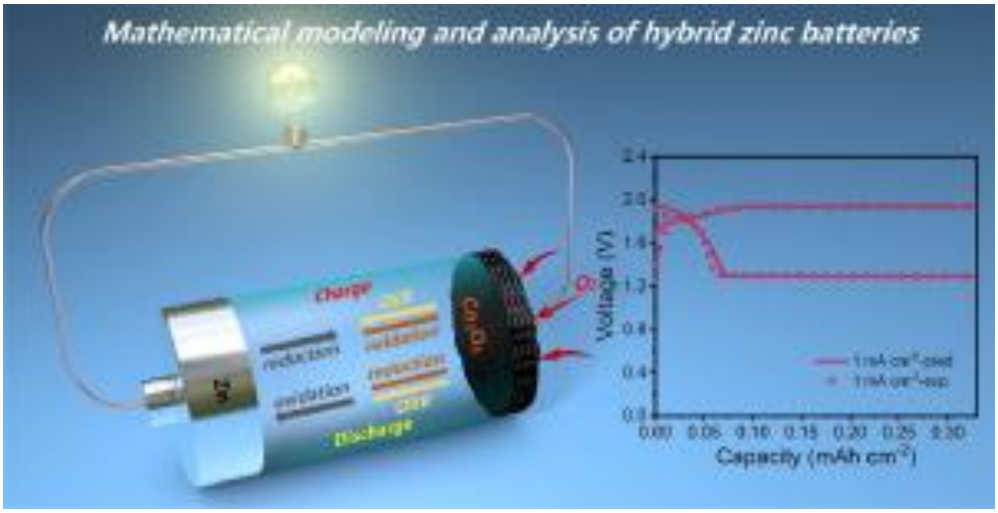

Keywords

Hybrid zinc battery

Aqueous electrolyte

Numerical analysis

Performance optimization

Nomenclature

a specific electroactive area ($m^2\ m^{-3}$)

c molar concentration ($mol\ m^{-3}$)

D diffusion coefficient ($m^2\ s^{-1}$)

E potential (V)

F Faraday constant (96,485 $C\ mol^{-1}$)

I applied current density ($A\ m^{-2}$)

i_{nj}
: transfer current density of reaction j (A m^{-2})

i_{oj}
: exchange current density of reaction j (A m^{-2})

JkmΓ
: interfacial species transfer rate due to interface movement (mol m^{-3} s^{-1})

Jkmd
: interfacial species transfer rate due to diffusion (mol m^{-3} s^{-1})

j
: transfer current density (A m^{-2})

k
: conductivity of liquid (S m^{-1})

m
: mass fraction of each solid-phase species, active material loading (mg cm^{-2})

M
: general chemical formula, molar density (mol m^{-3})

MW
: molecular weight of species (kg mol^{-1})

n
: number of transferred electron

P
: pressure (Pa)

Q
: source term

R
: reaction rate, universal gas constant (8.314 J mol^{-1} K^{-1})

T
: working temperature (K)

t
: time (s)

tk
: transference number of the electrolyte

t−o
: transference number of OH−

u
: velocity vector of gas mixture (m s^{-1})

v
: stoichiometric coefficient

w
: mass fraction of each gas-phase species

x
: molar fraction of each gas-phase species

X
: utilization ratio of the active material

Y
: capacity ratio of the Zn-air region

Greek

α
: charge transfer coefficient

η
: overpotential (V)

Φ
: electric potential (V)

ε
: porosity

ρ
: density (kg m^{-3})

Γ
: phase transformation rate (V)

κ
: permeability (m^2)

μ
: dynamic viscosity (Pa•s)

σ
: conductivity of solid matrix (S m^{-1})

ω
: energy density (W h kg^{-1})

Superscripts and subscripts

a
: anodic

c
: cathodic

D
: pertinent to diffusion

e
: electrolyte phase

eq
: equilibrium

eff
: effective

g
: gas phase

i
: different species

int
: initial value

j
: reaction j

k
: different species

o
: initial value, reference value

ref
: reference

s
: solid phase

se
: solid-electrolyte interface

z
: charge number

1. Introduction

The long-term dependence on conventional fossil fuels has led to serious energy crisis and environmental pollution. It is of great demand to look for energy-efficient and environmentally friendly energy storage and conversion systems [1], [2], [3], [4], [5]. Li-ion batteries are regarded as a compelling choice to meet these demands, which have been widely applied in electric/hybrid vehicles and other consumer electronics due to the excellent electrochemical properties [6], [7], [8], [9], [10]. However, barriers such as high cost and safety issues limit the large-scale applications [11].

Due to the advantages of low cost, excellent theoretical capacities, and high safety, zinc-based batteries with alkaline electrolytes are considered as alternatives to Li-ion batteries [12], [13], [14]. Until now, various kinds of zinc-based batteries have been rapidly developed, which can be classified into two categories based on the structure. One is a conventional Zn–M (M stands for transition metal oxide/hydroxide) battery with a closed structure, such as the Zn–Ag, Zn–Co, and Zn–Ni batteries [15], [16], [17], [18], [19], and the other is the Zn–air battery with a half-open system in which oxygen is absorbed from the surrounding atmosphere with taking up no mass or volume. Although conventional Zn–M batteries can deliver an excellent working voltage (e.g., ≈1.8 V of Zn–Ni batteries) [20], the discharge capacities are restricted by the positive active materials and are lower than that of metallic zinc. As for the Zn–air batteries, although the theoretical capacity depends on metallic zinc (820 mAh g^{-1}), the overpotential is usually large due to the sluggish reaction kinetics of oxygen reactions (ORR and OER) processes on the positive electrode, resulting in low energy efficiency (~55-65%), limited power densities, and poor rate capability [21], [22], [23], [24]. To addressed the above-mentioned issues, a novel hybrid zinc battery integrating the redox reactions of metal oxide/hydroxide in Zn-M batteries and the ORR/OER in Zn–air batteries at the cell level is proposed [25]. The positive active materials inside the Zn–M battery act as the bifunctional oxygen electrocatalysts for the Zn–air battery as well. Consequently, the hybrid battery combines the advantages of the high voltage of Zn–M batteries

and the remarkable discharge capacity of Zn–air batteries simultaneously [26]. For example, in Li and co-workers' work, the hybrid Zn–Ni/air battery with $NiO/Ni(OH)_2$ nanoflake as the active electrode material delivered a superior power density (2700 W kg^{-1}) and a remarkable energy density (980 W h kg^{-1}) [27]. Tan and coworkers proposed a hybrid zinc battery by using Co_3O_4 nanosheet-decorated carbon cloth as the active material, which showed a remarkable capacity of 792 mAh gZn−1 and a discharge voltage up to 1.85 V in the Zn–Co reaction region [28]. Li et al. presented a hybrid zinc battery constructed by the electrode of $NiCo_2O_4$ nanowire arrays, which delivered a decent working voltage of 1.7 V and outstanding cycle stability for over 5000 cycles [29]. All these works have promoted the development of hybrid zinc batteries. However, owing to the characteristics of two-stage reactions, several issues need to be clarified to further improve the performance: first, as the energy efficiency and energy density are determined by the two-stage reactions, the appropriate discharge depth should be investigated; second, since the two-stage reactions have different requirements on the reaction interfaces [25], the effects of different interfaces should be revealed; and third, the active material on the positive electrode is degraded gradually during cycling, while the effects on the long-term stability are still unknown.

To the best of our knowledge, the reported works related to hybrid zinc batteries have focused on experimental investigations. If the above questions are studied by means of experiments, it is time-consuming and laborious. On the other hand, some design parameters (e.g., reaction interfaces) are difficult to precisely control, resulting in the failure to obtain accurate results. Using mathematical models and numerical simulations can help to investigate the related problems effectively, which is crucial for performance improvement. So far, models of Zn–M batteries (e.g., Zn–Co battery [30]) and Zn–air batteries [31,32] have been developed, while the mathematical model of a hybrid zinc battery has not been reported yet.

Herein, a one-dimensional model coupling mass transport and energy conversion is established to predict the charge–discharge performance of a hybrid Zn–Co/air battery with Co_3O_4 as the active material. After validation, the impacts of key factors on the energy efficiency are investigated, including the discharge depth, reaction interfaces, and active material degradation during cycling. Additionally, the optimization scheme is proposed for performance improvement. This work is the first one using the numerical method to investigate hybrid zinc batteries, which is expected to effectively promote the development of this technology.

2. Model development

As illustrated in **Fig. 1**, a hybrid zinc battery is assembled using a zinc foil as the negative electrode, a Co_3O_4 nanosheet-decorated carbon cloth as the positive electrode, and an aqueous solution composed of 6 M potassium hydroxide (KOH) as the electrolyte [25]. The porous carbon cloth serves as a current collector and a gas diffusion layer through which oxygen can enter. The electrochemical reactions are demonstrated as:

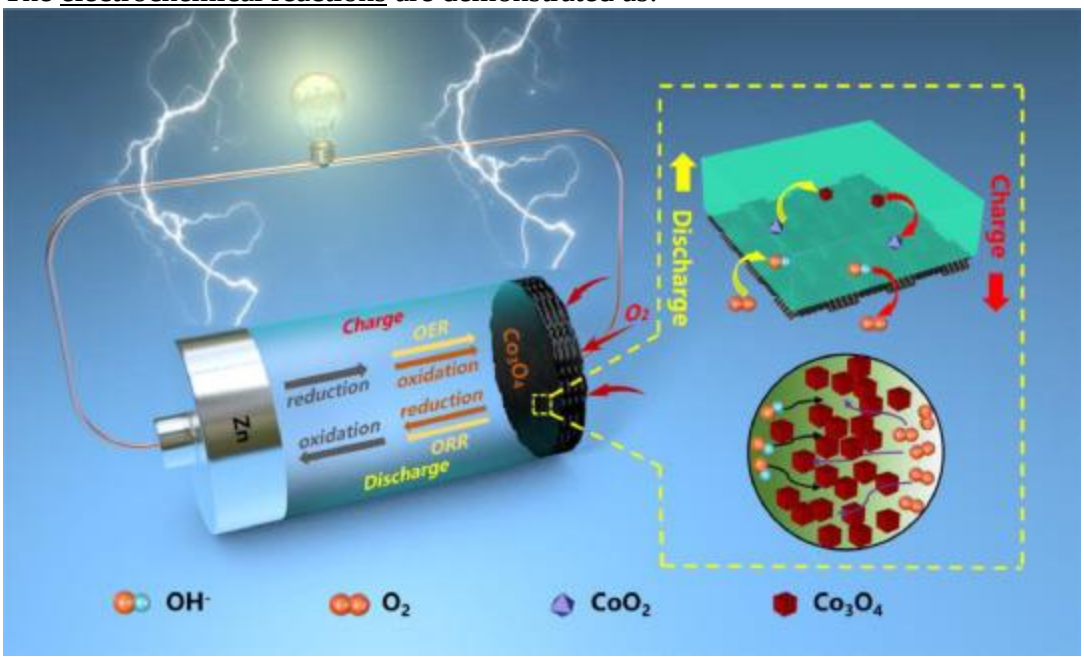

Fig. 1. Schematic diagram of a hybrid zinc battery using Co_3O_4 as the positive electrode material.

Positive electrode:

$$CoO_2 + H_2O + e^- \underset{\text{charge}}{\overset{\text{discharge}}{\rightleftharpoons}} CoOOH + OH^- \quad (I)$$

$$3CoOOH + e^- \underset{\text{charge}}{\overset{\text{discharge}}{\rightleftharpoons}} Co_3O_4 + OH^- + H_2O \quad (II)$$

$$O_2 + 2H_2O + 4e^- \underset{\text{charge}}{\overset{\text{discharge}}{\rightleftharpoons}} 4OH^- \quad (III)$$

Negative electrode:

$$Zn + 4OH^- \underset{\text{charge}}{\overset{\text{discharge}}{\rightleftharpoons}} [Zn(OH)_4]^{2-} + 2e^- \quad (IV)$$

For the positive electrode, in addition to the oxygen electrocatalysis (Reaction III) in the Zn-air reaction region, the redox reactions of cobalt oxide/hydroxide occur in the Zn–Co reaction region (Reactions I and II). Thus, Co_3O_4 acts as not only the active material for the Zn–Co reaction but also the bifunctional oxygen electrocatalysts for the Zn–air reaction. For the negative electrode, zinc reacts with OH^- anions to form $[Zn(OH)_4]^{2-}$ complex, and will be transformed into ZnO when the concentration reaches the saturation value. In this modeling work, we assumed the amount of electrolyte is high enough that $[Zn(OH)_4]^{2-}$ complex is dissolved. Based on this assumption, we can focus on the behaviors of the positive electrode of the hybrid zinc battery and neglect the effects of ZnO formation. For the sake of simplicity, we assumed that the mass convection inside the battery can be neglected, and the battery operates under an isothermal condition. A one-dimensional (1D) isothermal model is constructed, including three domains: the negative electrode surface, the separator, and the positive porous electrode.

2.1. Governing equations

The electrochemical reactions are demonstrated as:

$$\sum_{j} v_j M_j^{z_j} = n_j e^- \qquad (1)$$

where v_j and M_j represent the stoichiometric coefficient and the general chemical formula for each species, z_j and n_j denote the charge number and the number of transferred electrons, respectively. At the electrode/electrolyte interface, the reaction rate of species can be defined as:

$$R_{se} = -\sum_{j}\left(\frac{v_j}{n_j F} i_{nj}\right) \qquad (2)$$

where the electrochemical reaction rate is calculated by the Butler-Volmer equation [33]:

$$i_{nj} = i_{oj}\left\{\prod_i\left(\frac{c_i}{c_{i,ref}}\right)^{pi}\prod_k\left(\frac{M_k}{M_{k,ref}}\right)^{pk}\exp\left(\frac{\alpha_{aj} n_j F \eta}{RT}\right)\right.$$
$$\left.-\prod_i\left(\frac{c_i}{c_{i,ref}}\right)^{qi}\prod_k\left(\frac{M_k}{M_{k,ref}}\right)^{qk}\exp\left(\frac{-\alpha_{cj} n_j F \eta}{RT}\right)\right\} \qquad (3)$$

where i_{oj} denotes the exchange current density, M denotes the molar density, c and c_{ref} represent the concentrations of OH−ions at the reaction interface and in the reference state, separately. F, R, and T represent the Faraday's constant, universal gas constant, and working temperature,

respectively. αaj and αcj denote the anodic and cathodic charge transfer coefficients, which are determined by the following condition:

$$\alpha_{aj} + \alpha_{cj} = 1 \tag{4}$$

and the overpotential η is defined as:

$$\eta = \Phi_s - \Phi_e - E_{eq} \tag{5}$$

where Φs is the solid electrode potentials and Φe is the liquid electrolyte potentials. Eeq denotes the equilibrium potential for each reaction.

At the positive electrode, the total current is associated with Reactions I, II, and III. In consequence, the Butler-Volmer equations for each reaction are described as:

$$i_{n1} = i_{o1}\left\{\left(\frac{c_{OH}}{c_{OH,ref}}\right)\left(\frac{M_{CoOOH}}{M_{CoO_2,ref}}\right)\exp\left(\frac{\alpha_{a1}F\eta_1}{RT}\right) - \left(\frac{M_{CoO_2}}{M_{CoO_2,ref}}\right)\exp\left(\frac{-\alpha_{c1}F\eta_1}{RT}\right)\right\} \tag{6a}$$

$$i_{n2} = i_{o2}\left\{\left(\frac{c_{OH}}{c_{OH,ref}}\right)\left(\frac{M_{Co_3O_4}}{M_{CoOOH}}\right)\exp\left(\frac{\alpha_{a2}F\eta_2}{RT}\right) - \left(\frac{M_{CoOOH}}{M_{CoOOH,ref}}\right)^3\exp\left(\frac{-\alpha_{c2}F\eta_2}{RT}\right)\right\} \tag{6b}$$

$$i_{n3} = i_{o3}\left\{\left(\frac{c_{OH}}{c_{OH,ref}}\right)^4\exp\left(\frac{4\alpha_{a3}F\eta_3}{RT}\right) - \left(\frac{P_{O_2}}{P_{ref}}\right)\exp\left(\frac{-4\alpha_{c3}F\eta_3}{RT}\right)\right\} \tag{6c}$$

At the negative electrode, only Reaction IV occurs, the Butler-Volmer equation is shown below:

$$i_{n4} = i_{o4}\left\{\exp\left(\frac{2\alpha_{a4}F\eta_4}{RT}\right) - \exp\left(\frac{-2\alpha_{c4}F\eta_4}{RT}\right)\right\} \tag{6d}$$

2.1.1. Conservation of mass

The porosity change of the positive electrode can be determined by the mass balance shown below:

$$\frac{\partial \varepsilon_s}{\partial t} = -\frac{1}{F}\left(\frac{MW_{CoO_2}}{\rho_{CoO_2}} - \frac{MW_{CoOOH}}{\rho_{CoOOH}}\right)a_{Co_3O_4}i_{n,1}$$

$$-\frac{1}{F}\left(\frac{3MW_{CoOOH}}{\rho_{CoOOH}}-\frac{MW_{Co_3O_4}}{\rho_{Co_3O_4}}\right)a_{Co_3O_4}i_{n,2} \quad (7)$$

where *MW*, ρ, and *a* represent the molecular weight, the density, and the electroactive surface area, respectively. The right-hand side of the equation demonstrates the volumetric change of the positive electrode owing to the conversion of the active material CoO_2 to CoOOH (Reaction I) and CoOOH to Co_3O_4 (Reaction II) during discharge. The terms are reversed during the charge process. Using a Zn foil as the negative electrode in the experiment, which is set as an electrode surface in the model without considering the porosity change.

2.1.2. Conservation of species

The equation for the conservation of species is described as:

$$\frac{\partial(\varepsilon c_{OH})}{\partial t}=\nabla\cdot\left(D_k^{eff}\cdot\nabla c_{OH}\right)+\sum_m\left(J^{\Gamma}+J^{d}\right)-i^{\overrightarrow{OH}}\cdot\nabla\left(\frac{t_k}{zF}\right) \quad (8)$$

where tk represents the transference number of the electrolyte, the terms JΓ and Jd denote the interfacial transfers of species in the electrolyte owing to the interface movement and the microscopic diffusion, separately. The interfacial transport of species at the reaction interface is as follows:

$$J_{km}^{d}+J_{km}^{\Gamma}=-a_{km}\sum_j\left(\frac{t_k}{zF}+\frac{v_j}{n_jF}\right)\bar{i}_{nj} \quad (9)$$

Through simplification, the conservation of species is described as:

$$\frac{\partial(\varepsilon c_{OH})}{\partial t}=\nabla\cdot\left(D_{eff}^{OH}\nabla c_{OH}\right)-\left(\frac{t_-^o+1}{F}+\nabla\left(\frac{t_-^o}{zF}\right)\right)j^{OH} \quad (10)$$

For the Zn-air reaction, the gases transport inside the positive electrode is expressed by the Maxwell–Stefan equation [34]:

$$\nabla\left\{-\rho w_i\sum_{k=1}^{N}D_{ik}\left[\frac{M}{M_k}\left(\nabla w_k+w_k\frac{\nabla M}{M}\right)+(x_k-w_k)\frac{\nabla P}{P}\right]+w_i\rho\vec{u}\right\}=R_i \quad (11)$$

where D_{ik} denotes the binary diffusion coefficient, *w* and *x* represent the mass fraction and molar fraction of each gas-phase species, respectively. ρ_g denotes the gas mixture density defined by:

$$\rho_g = \left(\sum_i x_i \cdot M_i\right) P/(R \cdot T) \quad (12)$$

where R_i denotes the reaction rate, and for oxygen is described as:

$$R_{O_2} = -\frac{|i_{n3}|}{4F} M_{O_2} \quad (13)$$

The nitrogen can be approximately obtained from the mass balance equation:

$$w_{N_2} = 1 - w_{O_2} \quad (14)$$

The permeation of the gas mixture in the porous electrode can be described by the Darcy's law as [35]:

$$\frac{\partial(\varepsilon_g \rho)}{\partial t} + \nabla \cdot (\rho u) = Q \quad (15)$$

where u denotes the velocity vector of the gas mixture, Q is the source term, and u is calculated as:

$$u = -\frac{\kappa}{\mu} \nabla p \quad (16)$$

where μ represents the dynamic viscosity of the gas mixture, κ denotes the permeability.
The total current density is calculated through the following relations:

For the positive electrode:

$$j^{OH} = a_{Co_3O_4}(i_{n1} + i_{n2}) + a_{O_2} \cdot i_{n3} \quad (17a)$$

For the negative electrode:

$$j^{OH} = a_{Zn} i_{n4} \quad (17b)$$

The effective diffusion coefficient DoffOH in Eq. 10 is determined by the Bruggeman relation [36]:

$$D_{eff}^{OH} = \varepsilon_e^{1.5} D^{OH} \quad (18)$$

The binary diffusivities D_{ik} in Eq. 11 are obtained from the empirical correlation [34]:

$$D_{ik} = D_{ik\_o}\left(\frac{T}{T_o}\right)^{1.5} \quad (19)$$

where D_{ik_0} and T_0 represent the reference binary diffusivity and the reference temperature.

2.1.3. Conservation of electrical charge

The micro-macroscopic equations for the charge conservation are demonstrated as follows:

For the solid phase:

$$\nabla \cdot \left(\sigma^{\text{eff}} \nabla \Phi_{\text{s}}\right) + \sum_{\text{m}} I_{\text{sm}} = 0 \quad m \neq s \tag{20a}$$

For the electrolyte phase:

$$\nabla \cdot \left(k^{\text{eff}} \nabla \Phi_{\text{e}}\right) + \nabla \cdot \left(k_{\text{D}}^{\text{eff}} \nabla \ln c_{\text{OH}}\right) + \sum_{\text{m}} I_{\text{em}} = 0 \quad m \neq e \tag{20b}$$

where I_{sm} and I_{em} represent the interfacial current densities at the solid electrode and electrolyte interfaces, separately. Combining Eqs. 17a and 17b gives the following forms:

$$\nabla \cdot \left(\sigma^{\text{eff}} \nabla \Phi_{\text{s}}\right) - j^{\text{OH}} = 0 \tag{21a}$$

and

$$\nabla \cdot \left(k^{\text{eff}} \nabla \Phi_{\text{e}}\right) + \nabla \cdot \left(k_{\text{D}}^{\text{eff}} \nabla \ln c_{\text{OH}}\right) + j^{\text{OH}} = 0 \tag{21b}$$

Here, the effective conductivity (σ^{eff}) is modified based on the Bruggeman relation:

$$\sigma^{\text{eff}} = \sum_{\text{k}} \sigma_{\text{k}} m^{1.5} \tag{22}$$

where m denotes the mass fraction of each solid-phase species. Similarly, the effective electrolyte conductivity (k^{eff}) is defined as follows [36,37]:

$$k^{\text{eff}} = \frac{\varepsilon_{\text{e}} F^2}{RT} \left(D_{\text{K}^+} + D_{\text{OH}^-}\right) c_{\text{OH}} \tag{23}$$

2.2. Boundary conditions

At all outer boundaries in the electrolyte, the boundary conditions for potentials and concentrations are given as:(24)∂Φe∂n=∂c∂n=0

$$\frac{\partial \Phi_{\text{e}}}{\partial n} = \frac{\partial c}{\partial n} = 0 \tag{24}$$

In addition to the current collectors, $\frac{\partial \Phi_{\text{s}}}{\partial n} = 0$ is applied for the boundary condition for voltage in solid. At the zinc electrode, Φs=0 is applied for the reference voltage. As for the positive electrode current collector, $\frac{\partial \Phi_{\text{s}}}{\partial n} = -\frac{I}{\sigma^{\text{eff}}}$ is selected as the constant current condition (i=−iapp).

2.3. Model validation

The parameter values applied in this work and the other initial conditions adopted from the literature are given in **Table 1**. Using the COMSOL Multiphysics software, the mathematical model was established with the modules of binary electrolyte battery, transfer of concentrated species, and Darcy's law. The research was carried out under transient conditions. The convergence was determined by the relative tolerance of 10^{-3}. The cut-off voltages of discharge and charge processes were set to be 0.8 V and 2.2 V, respectively. Usually, the charge transfer coefficients are set as 0.5, while the values can be modulated to fit the experimental results, such as the anode transfer coefficient is set as 0.6 in the zinc-iron flow battery modeling [38] and 0.75 in the fuel cell modeling [34,39].

Table 1. Parameter values used in simulation.

Parameter	Symbol	Value	Unit	Ref.
Geometrical properties				
Thickness of the separator	L_{Sep}	5×10^{-3}	m	
Thickness of the positive electrode	L_{Pos}	3.3×10^{-4}	m	
Porosity of the separator	ε_{Sep}	0.5	-	
Porosity of the gas	ε_{gas}	0.4	-	
Porosity of the positive electrode	ε_{Pos}	0.8	-	
Specific surface area of the negative electrode	a_{Neg}	6×10^{6}	$m^2\ m^{-3}$	
Specific surface area of the two-phase interface	$a_{two\text{-}p}$	3×10^{7}	$m^2\ m^{-3}$	
Specific surface area of the three-phase interface	$a_{three\text{-}p}$	5×10^{6}	$m^2\ m^{-3}$	
Active material loading	m	3.06	mg cm^{-2}	[25]
Electrolyte properties				
Initial electrolyte concentration	cl,int	6000	mol m^{-3}	[25]
Reference electrolyte concentration	cOH,ref	6000	mol m^{-3}	[25]
Diffusion coefficient of OH^-	DOH−	5.77×10^{-9}	$m^2\ s^{-1}$	[37]
Diffusion coefficient of K^+	DK+	2.15×10^{-9}	$m^2\ s^{-1}$	[36]
Density of the electrolyte	ρ	1300	kg m^{-3}	
Transport number	t−o	0.38	-	

Gas properties				
Ambient pressure	P_{atm}	1.0133×10^{5}	Pa	
Permeability of gas mixture	κ	1×10^{-13}	m^2	
Dynamic viscosity of gas mixture	μ	3×10^{-5}	Pa•s	
Diffusion coefficient of gas mixture	D_{O2N2}	2.07×10^{-5}	$m^2\ s^{-1}$	
Inlet oxygen molar fraction	$x_{O2,in}$	0.21	-	
Reference pressure	P_{ref}	1.0133×10^{5}	Pa	
Kinetic parameter				
Exchange current density of reaction 1	i_{o1}	9×10^{-4}	$A\ m^{-2}$	
Exchange current density of reaction 2	i_{o2}	1	$A\ m^{-2}$	
Exchange current density of reaction 3	i_{o3}	5	$A\ m^{-2}$	
Exchange current density of reaction 4	i_{o4}	6×10^{-6}	$A\ m^{-2}$	
The anodic charge transfer coefficients of reaction 1	αa1	0.5	-	Assumed
The cathode charge transfer coefficients of reaction 1	αc1	0.5	-	Assumed
The anodic charge transfer coefficients of reaction 2	αa2	0.5	-	Assumed
The cathode charge transfer coefficients of reaction 2	αc2	0.5	-	Assumed
The anodic charge transfer coefficients of reaction 3	αa3	0.5	-	Assumed
The cathode charge transfer coefficients of reaction 3	αc3	0.5	-	Assumed
The anodic charge transfer coefficients of reaction 4	αa4	0.875	-	Assumed
The cathode charge transfer coefficients of reaction 4	αc4	0.125	-	Assumed
General parameter				
Density of Co_3O_4	ρCo3O4	6050	$kg\ m^{-3}$	
Density of CoO_2	ρCoO2	6450	$kg\ m^{-3}$	
Density of CoOOH	ρCoOOH	2900	$kg\ m^{-3}$	
Molar mass of Potassium ion	M_{K+}	39.1	$g\ mol^{-1}$	

Molar mass of OH ion	M_{OH-}	17.0	g mol^{-1}	
Molar mass of solvent	M_{H20}	18.0	g mol^{-1}	
Molar mass of O_2	MW_{O2}	32.0	g mol^{-1}	
Molar mass of N_2	MW_{N2}	28.0	g mol^{-1}	
Molecular weight of Co_3O_4	MW_{Co3O4}	240.79	g mol^{-1}	
Molecular weight of CoO_2	MW_{CoO2}	90.93	g mol^{-1}	
Molecular weight of CoOOH	MW_{CoOOH}	91.93	g mol^{-1}	
Conductivity of Co_3O_4	σ_{Co3O4}	5×10^{-3}	S m^{-1}	
Conductivity of CoO_2	σ_{CoO2}	2×10^{-2}	S m^{-1}	
Conductivity of CoOOH	σ_{CoOOH}	8×10^{-3}	S m^{-1}	
Conductivity of Zn	σ_{Zn}	1.83×10^{7}	S m^{-1}	
Conductivity of ZnO	σ_{ZnO}	1	S m^{-1}	
Operating temperature	T	300	K	
Number of transferred electrons of reaction 1	n_1	1	-	
Number of transferred electrons of reaction 2	n_2	1	-	
Number of transferred electrons of reaction 3	n_3	2	-	
Number of transferred electrons of reaction 4	n_4	4	-	
Equilibrium potential of reaction1	Eeq1	0.56	V	[40]
Equilibrium potential of reaction2	Eeq2	0.35	V	[40]
Equilibrium potential of reaction3	Eeq3	-1.45	V	[40]
Equilibrium potential of reaction4	Eeq4	0.401	V	[24]
Initial concentration of CoOOH	cCoOOH,init	1×10^{-5}	mol m^{-3}	
Initial concentration of CoO_2	cCoO2,init	60	mol m^{-3}	

The discharge–charge curves of the hybrid zinc batteries are compared with the experimental data under the same working conditions at a current density of 1 mA cm^{-2}. As illustrated in **Fig. 2**, a good agreement between the simulation results and the experimental data is demonstrated. The difference in the initial stage of charge and discharge process may come from the conductivity change of the positive electrode due to the activation in the actual working process. It is noting that the discharge voltage corresponding to the oxidation reaction of cobalt oxide lacks a plateau, and the reasons are as follows: the active materials are consumed continuously during the discharge process, which leads to the changes of electrical conductivity and reaction active area.

Consequently, the discharge voltage is continuously decreasing, which is consistent with experimental results [40]. From the validation results, the 1D isotherm model displays excellent accuracy and therefore can be applied for predicting the charge-discharge characteristics of a hybrid zinc battery.

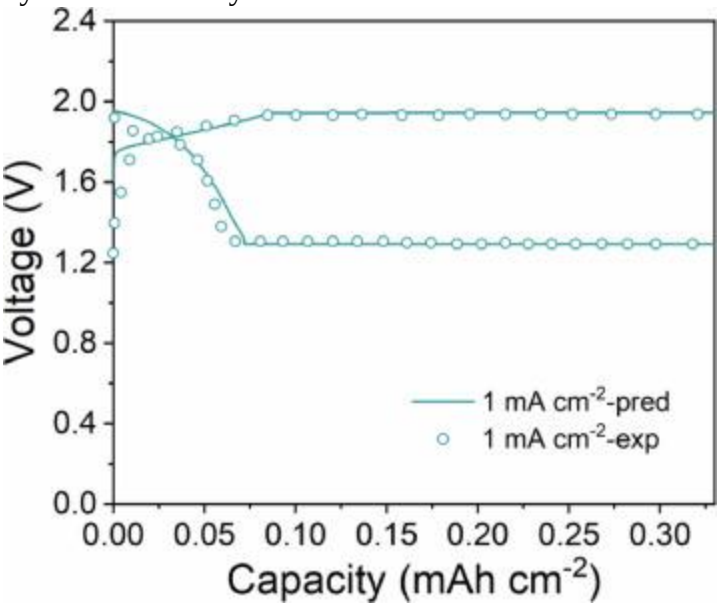

Fig. 2. Comparisons of the simulated voltage curves of a hybrid zinc battery with the experimental data from Ref. [25].

3. Results and discussion

In this section, the effects of discharge depth, reaction interfaces, and active material degradation on energy efficiency are analyzed in detail based on the developed model.

3.1. Effects of discharge depth

Fig. 3a exhibits the discharge-charge curves of a hybrid zinc battery at the current densities of 1, 2, and 4 mA cm^{-2}. As the current density increases, the capacity of the Zn–Co region decreases, while the discharge-charge voltage gaps for both Zn–air and Zn–Co regions increase. At a high discharge rate, the polarization inside the battery is enhanced, resulting in the low Zn–Co capacity and discharge voltage. **Fig. 3b** exhibits the relationship between the energy efficiency and discharge depth at different current densities, from which the energy efficiency of the Zn–Co reaction is high and gradually decreases with an increase of the depth, and finally becomes stable with the progress of the Zn–air reaction. Meanwhile, the energy efficiency significantly decreases with an increase of the discharge rate. When the capacity reaches 0.8 mAh cm^{-2}, the energy

efficiency is stable, which means that the effect of the Zn–Co reaction region becomes negligible. At this point, the energy efficiency is 68.88%, 62.92%, and 57.38% at the current density of 1, 2, and 4 mA cm^{-2}, respectively. **Fig. 3c** exhibits the change of energy density with discharge depth at different current densities based on the weight of zinc and Co_3O_4. At a given discharge depth, the higher the current density, the lower the energy density. Besides, the energy density increases with the discharge capacity, while the increasing trend gradually slows down, and finally tends to a constant. Thus, the energy density contributed by the Zn–Co reaction region becomes limited under the circumstance of sufficient zinc and deep discharge. However, to avoid the failure of reaction boundaries inside the rechargeable Zn–air batteries, a fixed capacity is usually set for charge–discharge cycles [41]. At a given discharge depth, the Zn–Co reaction can greatly affect the charge-discharge voltages (e.g., when the ratio of Zn–Co reaction is high). To obtain optimal energy efficiency and energy density in practical applications, the discharge depth can be modulated by controlling the amount of zinc.

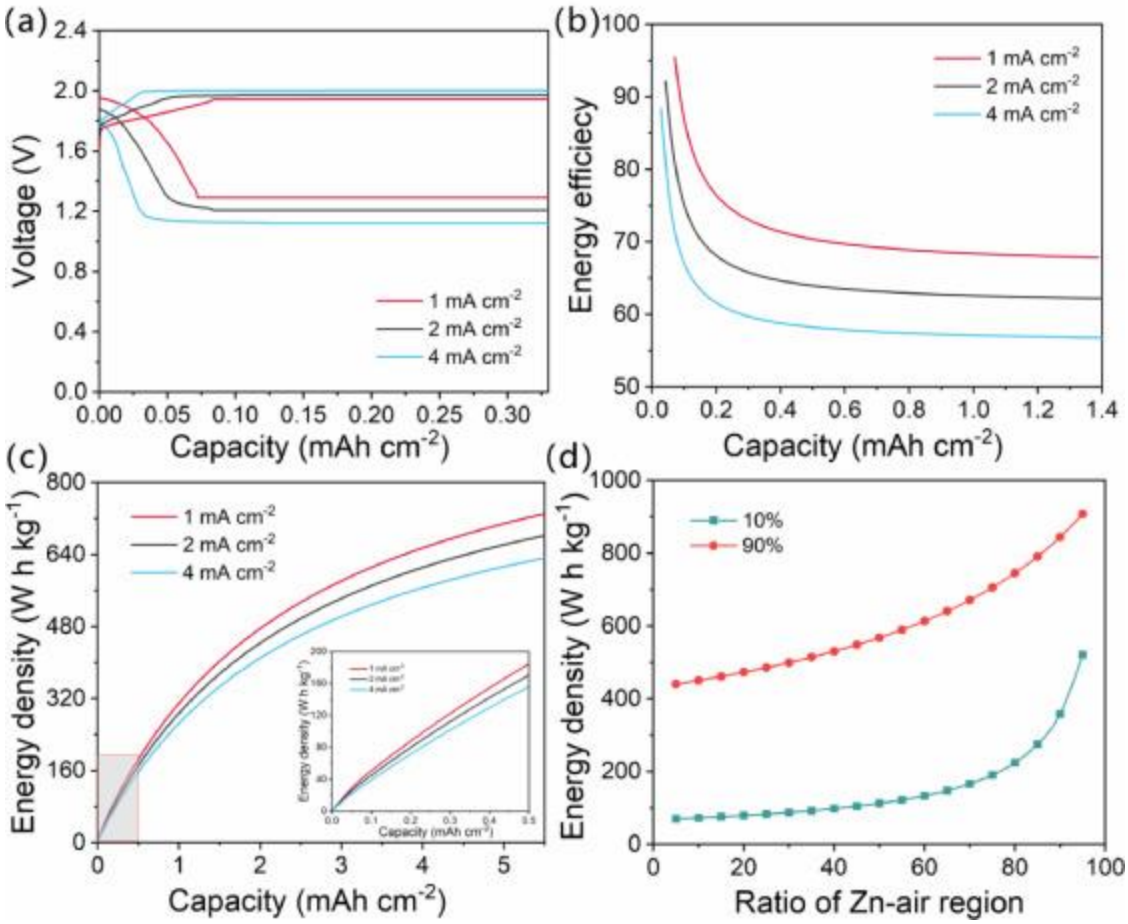

Fig. 3. (a) Discharge–charge curves (b) The change of energy efficiency with the discharge depth (c) The change of energy density with the discharge depth at different current

densities. (d) The change of energy density with the capacity ratio of the Zn–air reaction at different utilization ratios of the active material.

The selection of discharge depth mainly depends on the utilization ratio of the active materials and the capacity ratio of the Zn–air reaction. In this work, when the discharge capacity is 0.14 mAh cm^{-2} (the discharge capacity of Zn–Co and Zn–air reactions each contributes 50%), the superior energy efficiency (80.78%) can be obtained at the current density of 1 mA cm^{-2}, while the energy density (65.78 W h kg^{-1}) is relatively low. It is because the energy density contributed by the Zn–Co reaction is extremely low due to the low utilization ratio (e.g., ~5%) [40]. The relationship between the energy density and the capacity ratio of the Zn-air reaction at different utilization ratios of the active material is indicated in **Fig. 3d**, from which the utilization ratio of the active material can greatly affect the energy density. When the utilization ratio of the active material is a constant, the energy density increases with the capacity ratio of the Zn-air reaction, whereas the energy efficiency decreases. The details are shown in the appendix. To sum up, the utilization ratio of active materials should be increased as high as possible.

3.2. Effects of reaction interface

The gas-involved electrochemical reactions (ORR and OER) in the Zn–air region take place at the solid–liquid–gas triple-phase interfaces, as shown in **Fig. 1**, which are of great importance for the battery performance, while the Zn–Co reactions occur at the solid–liquid two-phase interfaces. The difference in interface requirements between two-stage reactions in a hybrid zinc battery is an important factor affecting battery performance. To this end, we studied the ratio of two-phase and three-phase interfaces and the degradation of three-phase interfaces during cycling. The discharge depth with a capacity of 0.14 mAh cm^{-2} is set for discharge-charge cycles in which the Zn–air and Zn–Co reactions contribute equally.

3.2.1. Two-phase and three-phase interfaces on energy efficiency

To investigate the relationship between two-phase and three-phase interfaces, the ratio of these two kinds of interfaces is modulated while the total area of the interfaces is set to be constant. **Fig. 4a** exhibits the discharge–charge curves of a hybrid zinc battery under different ratios of two-phase and three-phase interfaces. With a decrease of the ratio of two-phase and three-phase interfaces, the capacity of the Zn–Co region decreases but the discharge voltage of the Zn–air region increases. This is because that the decrease of the two-phase interfaces results in the

shrinkage of active material concentration in the Zn–Co reaction, while increasing the three-phase interfaces can exposure more active sites for the ORR process, leading to the enhanced electrochemical reaction rate of the Zn–air reaction. While for the charge process, the OER can occur at the solid–liquid interface without the requirement of gaseous oxygen transport channels. To this end, the interface changes have a limited effect on the charge voltage of the Zn–air region, which is also consistent with the experimental results [25]. As illustrated in **Fig. 4b**, the energy efficiency of the hybrid battery decreases with a decreased ratio of two-phase and three-phase interfaces. Owing to the capacity loss of the Zn–Co region cannot be compromised by the voltage increase of the Zn–air region, the influence of the two-phase interfaces on the energy efficiency is greater than that of the three-phase interfaces at this given discharge depth. It is worth noting that with a great shrinkage of three-phase interfaces, the discharge voltage of the Zn–air region can be extremely low (e.g., <0.4 V) [28] owing to the absence of channels for gaseous oxygen transport. Thus, the ratio of two-phase and three-phase interfaces should be maintained in a proper region. When the discharge voltage of the Zn–air region ranges from 1.29 V to 1.37 V in the calculation case, the higher ratio of two-phase and three-phase interfaces can lead to higher energy efficiency.

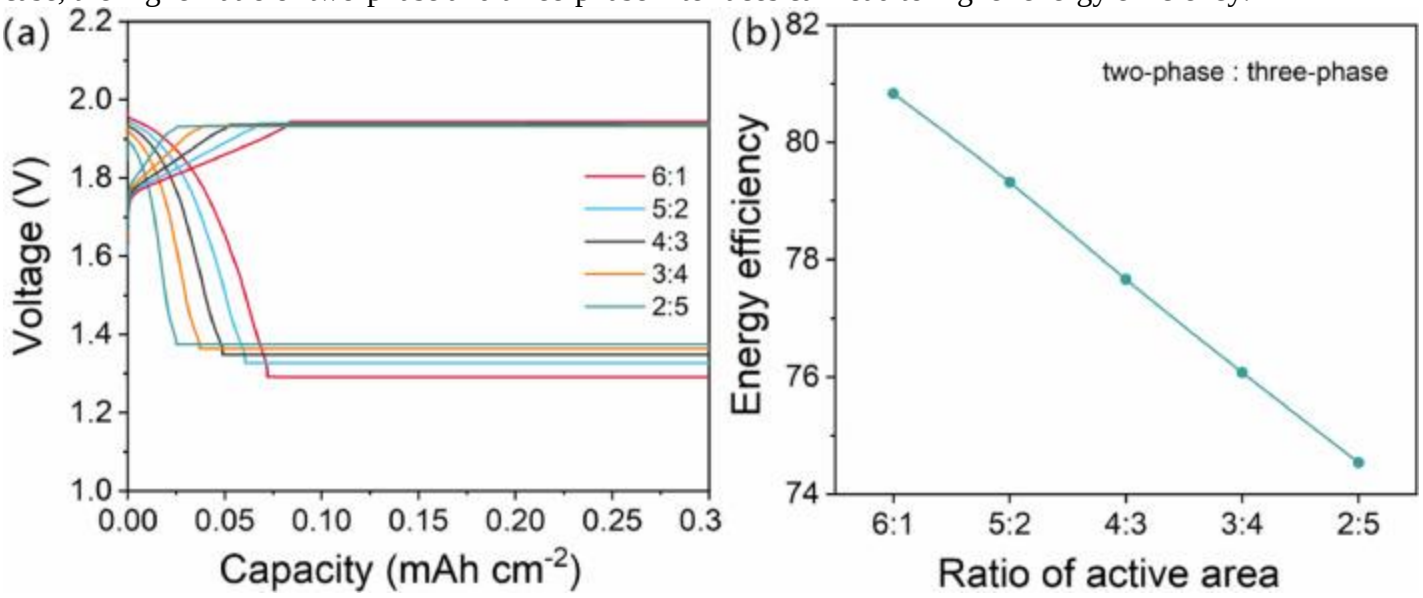

Fig. 4. (a) Discharge–charge curves under different ratios of two-phase and three-phase interfaces. (b) The change of energy efficiency with the ratio of reaction interfaces.

3.2.2. Decay of three-phase interface on the performance

The solubility of oxygen in the alkaline solution is low, which greatly impedes the accessibility of gas reactants. Thus, the hydrophobic additives like polytetrafluoroethylene (PTFE) are widely applied in the positive electrode of Zn–air batteries to build a gas transport channel, which can

improve the gas diffusion kinetics. However, the PTFE may be detached from the positive electrode and the gas transport channels would be flooded with electrolyte, resulting in the decay of three-phase interfaces during cycling [42]. **Fig. 5a** exhibits the discharge-charge curves of a hybrid zinc battery at different cycle numbers with the decay of three-phase interfaces of 20% after 1000 cycles. The capacity of the Zn–Co region increases and the discharge voltage of the Zn–air region decreases with an increasing number of cycles, while the charge voltage of the Zn-air region increases slightly. As illustrated in **Fig. 5b**, the voltage curves of the decay rate of 50% after 1000 cycles show the same trend, but the changes are more significant. As the cycle goes on, the three-phase interfaces decay gradually, and two-phase interfaces increase, which means more active materials (Co_3O_4) contact with the electrolyte, resulting in a higher discharge capacity of the Zn–Co region. However, the decrease of active sites of the Zn–air reaction leads to a further increase of charge–discharge voltage gaps. **Fig. 5c** and **5d** demonstrates the change of the capacity of the Zn–Co region and the energy efficiency with the cycle, respectively. Both of them exhibit a linearly increasing relationship and the voltage loss of the Zn–air region can be compromised by the capacity increase of the Zn–Co region. What is noteworthy is that with significant shrinkage of three-phase interfaces, the discharge voltage of the Zn–air region can be pretty low (e.g., <0.4 V) [28] owing to the absence of channels for gaseous oxygen transport. Thus, the decay of three-phase interfaces should be within a proper region. When the discharge voltage of the Zn–air region ranges from 1.25 V to 1.29 V in the calculation case, the decay of the three-phase interfaces is beneficial to the improvement of energy efficiency.

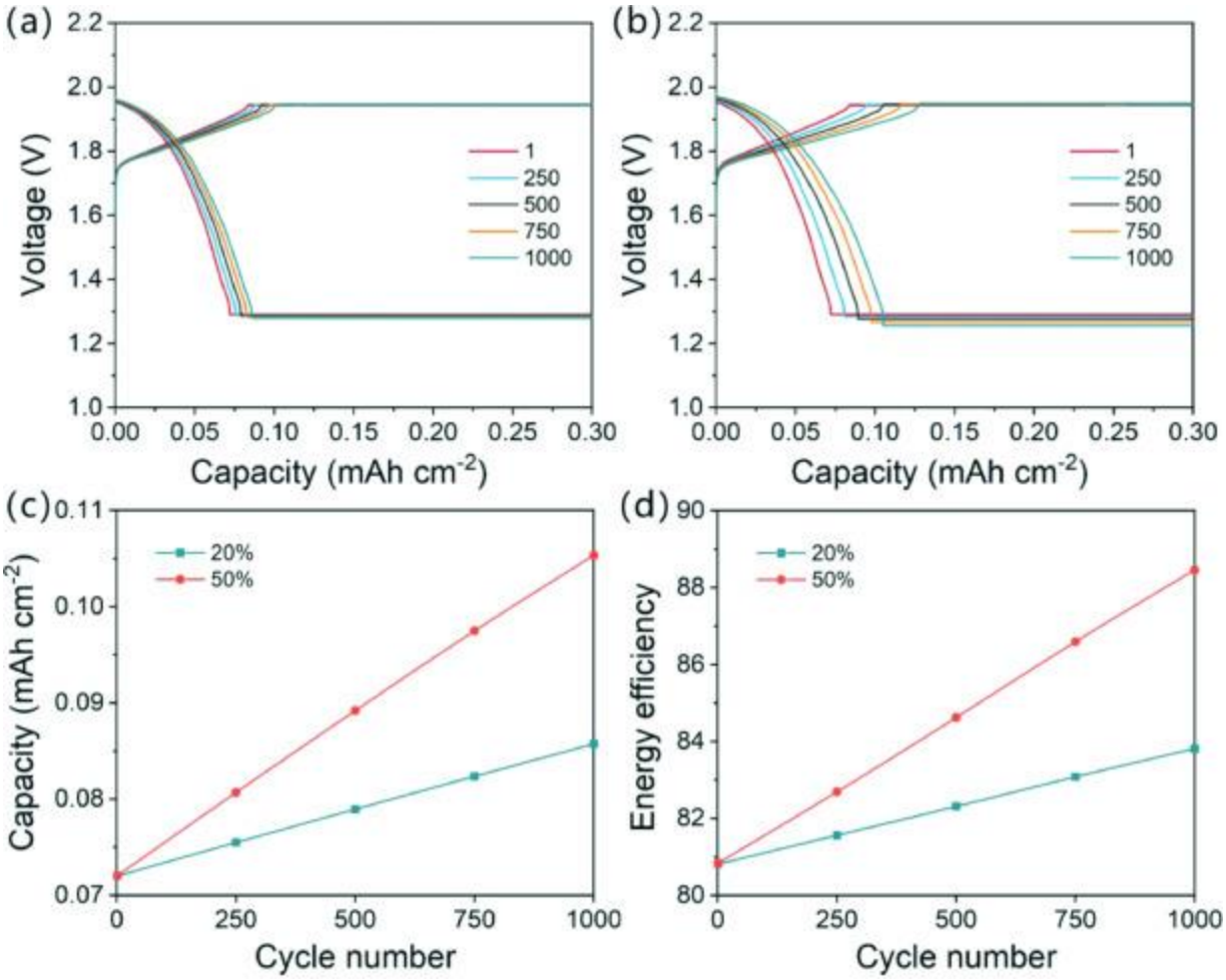

Fig. 5. Discharge–charge curves of the 1st, 250th, 500th, 750th, 1000th cycle under the condition that the three-phase interfaces decay by (a) 20% (b) 50% after 1000 cycles. (c) The change of the capacity of the Zn–Co reaction during cycling. (d) The change of the energy efficiency during cycling.

3.3. Effects of the decay of active materials

Many factors can contribute to the degradation of active materials, such as the physical structure change (e.g., grain growth) and chemical/electrochemical decomposition (e.g., carbon corrosion) [43,44]. The degradation of active materials during cycling greatly affects the performance of the batteries. For example, the degradation of active materials leads to a decrease of reaction interfaces, which in turn leads to a decrease of the reaction rate. The effects of the degradation of active materials on the performance during cycling are investigated here by setting a fixed capacity of 0.14 mAh cm^{-2}.

Fig. 6a exhibits the discharge-charge curves of a hybrid zinc battery at different cycle numbers with the decay of active materials of 20% after 1000 cycles. Both the capacity of the Zn–Co region and the discharge voltage of the Zn–air region decrease with the increasing number of cycles, while the charge voltage increases slightly. As shown in **Fig. 6b**, the voltage curves of the decay rate of 50% after 1000 cycles indicate the same trend, but the changes are more significant. When the active materials decay, both the two-phase and three-phase interfaces decrease, so does the reaction rate. **Fig. 6c** and **6d** demonstrates the change of the Zn–Co capacity and the energy efficiency with the cycle, respectively, from which the linearly decreasing relationship is exhibited. At the degradation of 50% after 1000 cycles, the energy efficiency reduces from 80.85 to 69.91, which is significant. In consequence, it is essential to suppress the degradation of active materials, such as using a binder-free electrode [45,46], dispersing nanoparticles over porous carbon host [47] or doping elemental into oxide support [48].

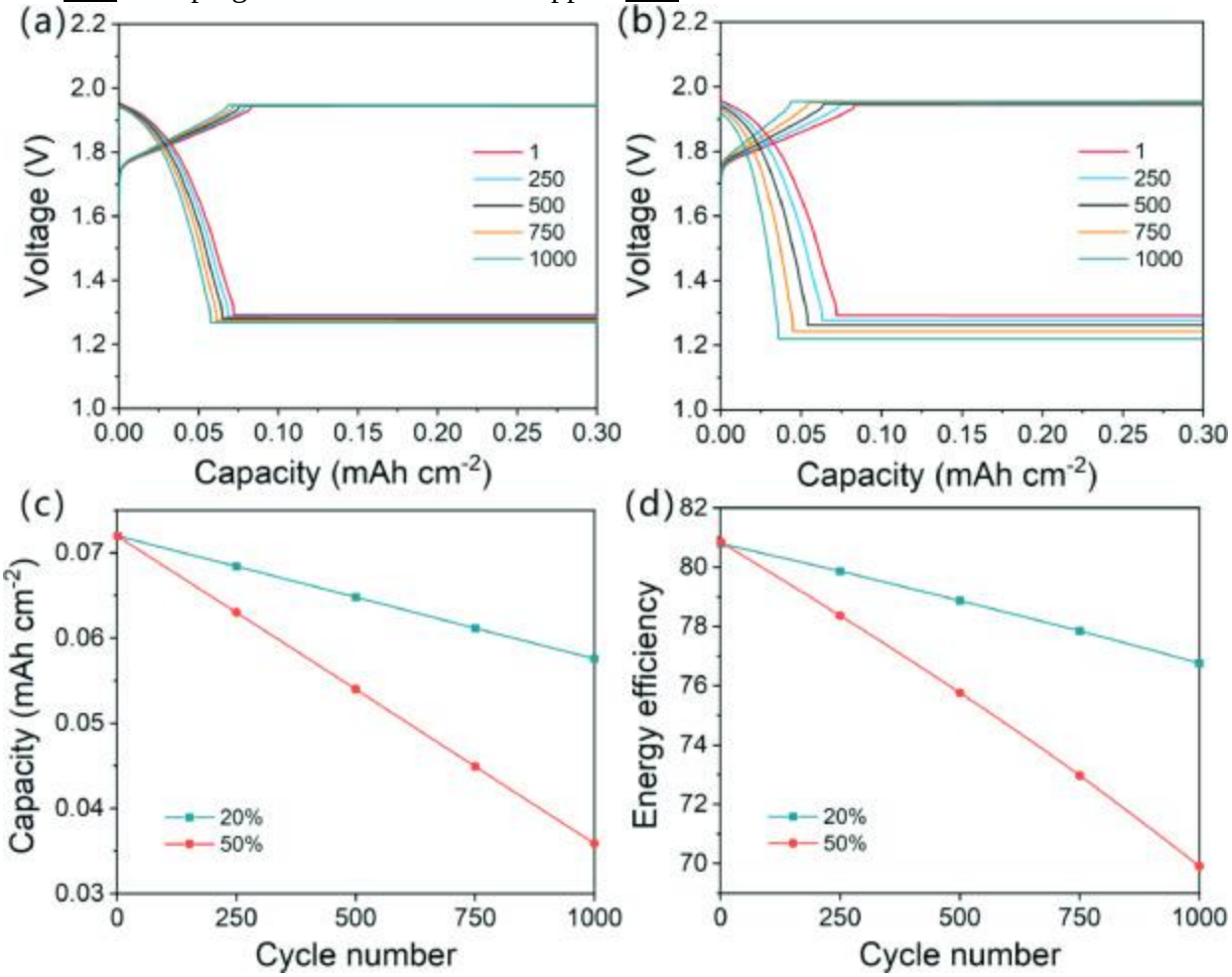

Fig. 6. Discharge–charge curves of the 1st, 250th, 500th, 750th, 1000th cycle under the condition that the active materials decay by (a) 20% (b) 50% after 1000 cycles. (c) The

change of the capacity of the Zn–Co reaction during cycling. (d) The change of the energy efficiency during cycling.

4. Conclusions

In summary, a one-dimensional isothermal model has been established to predict the charge–discharge performance of an alkaline hybrid zinc battery. The simulation curves demonstrate excellent agreement with the experiment results, indicating the high accuracy of the model. Using this model, the impacts of discharge depth, reaction interfaces, and active material degradation on energy efficiency are analyzed in detail. The results indicate that the larger discharge rate can lead to lower energy efficiency and density. The energy efficiency decreases rapidly in the initial stage and gradually becomes stable. The energy density increases with the discharge capacity, while the increasing trend gradually slows down, and finally tends to a constant. When the three-phase interfaces are within a proper region, the higher ratio of two-phase and three-phase interfaces can lead to higher energy efficiency, and the increase of the two-phase interfaces is beneficial for improving energy efficiency. While the effects of the degradation of active material on energy efficiency are significant, resulting in poor cycling stability. The work is favorable for the design of interfaces and the selection of operating conditions, and guides the performance improvement of hybrid zinc batteries. Meanwhile, the conclusions obtained can also inspire the development of other hybrid batteries such as a hybrid Zn–Mn/air battery with a neutral electrolyte [49].

Declaration of Competing Interest

None.

Acknowledgments

P. Tan thanks the funding support from Anhui Provincial Natural Science Foundation (2008085ME155), CAS Pioneer Hundred Talents Program (KJ2090130001), USTC Research Funds of the Double First-Class Initiative (YD2090002006), Joint Laboratory for USTC and Yanchang Petroleum (ES2090130110), and USTC Tang Scholar (KY2090000065). M. Ni thanks the funding support (Project Number: PolyU 152214/17E and PolyU 152064/18E) from Research Grant Council, University Grants Committee, Hong Kong SAR.

Appendix.

Assuming that the active material loading is mCo3O4, the capacity of the Zn–air region accounts for the ratio of *Y* in the discharge capacity, the utilization ratio of the active material is *X*. From the discharge voltage curves, the average voltage of the Zn–Co region is set to be 1.6 V, and the average voltage of the Zn–air region is set to be 1.2 V. Thus, the energy density of these two reaction regions can be expressed as

$$E_{\mathrm{Zn-air}} = \frac{X \cdot m_{\mathrm{Co_3O_4}} \cdot 446\,\mathrm{mAh\,g^{-1}}}{1-Y} \cdot Y \cdot 1.2\,\mathrm{V} \quad (A1)$$

$$E_{\mathrm{Zn-Co}} = X \cdot m_{\mathrm{Co_3O_4}} \cdot 446\,\mathrm{mAh\,g^{-1}} \cdot 1.6\,\mathrm{V} \quad (A2)$$

$$m_{\mathrm{Zn}} = \frac{X \cdot m_{\mathrm{Co_3O_4}} \cdot 446\,\mathrm{mAh\,g^{-1}}}{(1-Y) \cdot 820\,\mathrm{mAh\,g^{-1}}} \quad (A3)$$

The energy density of the hybrid battery ω is defined as:

$$\omega = \frac{E_{\mathrm{Zn-air}} + E_{\mathrm{Zn-Co}}}{m_{\mathrm{Zn}} + m_{\mathrm{Co_3O_4}}} = \frac{(1312 - 328Y) \cdot X}{X + 1.84(1-Y)}\,\mathrm{Wh\,kg^{-1}} \quad (A4)$$

which is dependent on the utilization ratio of the active material and the capacity ratio of the Zn–air reaction.

References

[1] B. Dunn, H. Kamath, J.M. Tarascon, B. Dunn, H. Kamath, J.-M. Tarascon
Electrical energy storage for the grid: a battery of choices
Science, 334 (2011), pp. 928-935
View PDF
CrossRefGoogle Scholar

[2] P. Tan, B. Chen, H. Xu, H. Zhang, W. Cai, M. Ni, M. Liu, Z. Shao
Flexible Zn- and Li-air batteries: recent advances, challenges, and future perspectives
Energy Environ. Sci., 10 (2017), pp. 2056-2080
View Record in ScopusGoogle Scholar

[3] S.C. Singhal
Advances in solid oxide fuel cell technology
Solid State Ionics, 135 (2000), pp. 305-313
ArticleDownload PDFView Record in ScopusGoogle Scholar

[4] A. Yoshino
The birth of the lithium-ion battery
Angew. Chem. Int. Ed., 51 (2012), pp. 5798-5800
CrossRefView Record in ScopusGoogle Scholar

[5] R. Marom, S.F. Amalraj, N. Leifer, D. Jacob, D. Aurbach
A review of advanced and practical lithium battery materials

J. Mater. Chem., 21 (2011), pp. 9938-9954
CrossRefView Record in ScopusGoogle Scholar
[6] C.M. Doherty, R.A. Caruso, C.J. Drummond
High performance $LiFePO_4$ electrode materials: influence of colloidal particle morphology and porosity on lithium-ion battery power capability
Energy Environ. Sci., 3 (2010), pp. 813-823
View PDF
CrossRefView Record in ScopusGoogle Scholar
[7] C. Wang, H. Wu, Z. Chen, M.T. Mcdowell, Y. Cui, Z. Bao
Self-healing chemistry enables the stable operation of silicon microparticle anodes for high-energy lithium-ion batteries
Nat. Chem., 5 (2013), pp. 1042-1048
View PDF
CrossRefView Record in ScopusGoogle Scholar
[8] R. Schmuch, R. Wagner, G. Hörpel, T. Placke, M. Winter
Performance and cost of materials for lithium-based rechargeable automotive batteries
Nat. Energy, 3 (2018), pp. 267-278
CrossRefView Record in ScopusGoogle Scholar
[9] L. Lu, X. Han, J. Li, J. Hua, M. Ouyang
A review on the key issues for lithium-ion battery management in electric vehicles
J. Power Sources, 226 (2013), pp. 272-288
ArticleDownload PDFGoogle Scholar
[10] S. Guo, J. Liu, Q. Zhang, H. Wang
3D porous $ZnCo_2O_4/Co_3O_4$ composite grown on carbon cloth as high-performance anode material for lithium-ion battery
Mater. Lett., 267 (2020), Article 127549
ArticleDownload PDFView Record in ScopusGoogle Scholar
[11]
N. Choi, Z. Chen, S.A. Freunberger, X. Ji, K. Sun, K. Amine, G. Yushin, L.F. Nazar, J. Cho, P.G. Bruce
Challenges facing lithium batteries and electrical double-layer capacitors angewandte
Angew. Chem. Int. Ed., 51 (2012), pp. 9994-10024
View PDF
CrossRefView Record in ScopusGoogle Scholar
[12] Y. Li, H. Dai
Recent advances in Zinc-air batteries
Chem. Soc. Rev., 43 (2014), pp. 5257-5275
View Record in ScopusGoogle Scholar
[13] J.F. Parker, J.S. Ko, D.R. Rolison, J.W. Long
Translating materials-level performance into device-relevant metrics for zinc-based batteries
Joule, 2 (2018), pp. 2519-2527
ArticleDownload PDFView Record in ScopusGoogle Scholar
[14] D. Selvakumaran, A. Pan, S. Liang, G. Cao

A review on recent developments and challenges of cathode materials for rechargeable aqueous Zn-ion batteries
J. Mater. Chem. A, 7 (2019), pp. 18209-18236
View PDF
CrossRefView Record in ScopusGoogle Scholar

[15] P. Tan, B. Chen, H. Xu, W. Cai, M. Liu, Z. Shao, M. Ni
Nanoporous NiO/Ni(OH)$_2$ plates incorporated with carbon nanotubes as active materials of rechargeable hybrid zinc batteries for improved energy efficiency and high-rate capability
J. Electrochem. Soc., 165 (2018), pp. A2119-A2126
View PDF
CrossRefView Record in ScopusGoogle Scholar

[16] X. Wang, M. Li, Y. Wang, B. Chen, Y. Zhu, Y. Wu
A Zn-NiO rechargeable battery with long lifespan and high energy density
J. Mater. Chem. A, 3 (2015), pp. 8280-8283
View PDF
CrossRefView Record in ScopusGoogle Scholar

[17] P. Tan, B. Chen, H. Xu, W. Cai, W. He, H. Zhang, M. Liu, Z. Shao, M. Ni
Integration of Zn−Ag and Zn−Air batteries: a hybrid battery with the advantages of both
ACS Appl. Mater. Interfaces, 10 (2018), pp. 36873-36881
View PDF
CrossRefView Record in ScopusGoogle Scholar

[18]
D. Ozgit, P. Hiralal, G.A.J. Amaratunga
Improving performance and cyclability of zinc-silver oxide batteries by using graphene as a two dimensional conductive additive
ACS Appl. Mater. Interfaces, 6 (2014), pp. 20752-20757
View PDF
CrossRefView Record in ScopusGoogle Scholar

[19]R. Kumar, J. Shin, L. Yin, J.M. You, Y.S. Meng, J. Wang
All-printed, stretchable Zn-Ag$_2$O rechargeable battery via hyperelastic binder for self-powering wearable electronics
Adv. Energy Mater., 7 (2017), Article 1602096
View PDF
CrossRefGoogle Scholar

[20] H. Chen, Z. Shen, Z. Pan, Z. Kou, X. Liu, H. Zhang, Q. Gu, C. Guan, J. Wang
Hierarchical micro-nano sheet arrays of nickel–cobalt double hydroxides for high-rate Ni–Zn batteries
Adv. Sci., 6 (2019), Article 1802002
View PDF
CrossRefView Record in ScopusGoogle Scholar

[21] Y. Shi, Y. Chen, L. Shi, K. Wang, B. Wang, L. Li, Y. Ma, Y. Li, Z. Sun, W. Ali, S. Ding
An overview and future perspectives of rechargeable zinc batteries
Small, 16 (2020), pp. 1-28

Google Scholar
[22] W. Shang, W. Yu, Y. Liu, R. Li, Y. Dai, C. Cheng, P. Tan, M. Ni
Rechargeable alkaline zinc batteries: progress and challenges
Energy Storage Mater, 31 (2020), pp. 44-57
ArticleDownload PDFView Record in ScopusGoogle Scholar
[23] S. Ren, X. Duan, S. Liang, M. Zhang, H. Zheng
Bifunctional electrocatalysts for Zn-air batteries: recent developments and future perspectives
J. Mater. Chem. A, 8 (2020), pp. 6144-6182
View PDF
CrossRefView Record in ScopusGoogle Scholar
[24] Y. Sun, X. Liu, Y. Jiang, J. Li, J. Ding, W. Hu, C. Zhong
Recent advances and challenges in divalent and multivalent metal electrodes for metal-air batteries
J. Mater. Chem. A, 7 (2019), pp. 18183-18208
View PDF
CrossRefView Record in ScopusGoogle Scholar
[25] P. Tan, B. Chen, H. Xu, W. Cai, W. He, M. Ni
Investigation on the electrode design of hybrid Zn-Co_3O_4 /air batteries for performance improvements
Electrochim. Acta, 283 (2018), pp. 1028-1036
ArticleDownload PDFView Record in ScopusGoogle Scholar
[26] W. Shang, W. Yu, P. Tan, B. Chen, Z. Wu, H. Xu, M. Ni
Achieving high energy density and efficiency through integration: progress in hybrid zinc batteries
J. Mater. Chem. A, 7 (2019), pp. 15564-15574
View PDF
CrossRefView Record in ScopusGoogle Scholar
[27] D.U. Lee, J. Fu, M.G. Park, H. Liu, A. Ghorbani Kashkooli, Z. Chen
Self-assembled NiO/$Ni(OH)_2$ nanoflakes as active material for high-power and high-energy hybrid rechargeable battery
Nano Lett., 16 (2016), pp. 1794-1802
View PDF
CrossRefView Record in ScopusGoogle Scholar
[28] P. Tan, B. Chen, H. Xu, W. Cai, W. He, M. Liu, Z. Shao, M. Ni
Co_3O_4 nanosheets as active material for hybrid Zn batteries
Small, 1800225 (2018), pp. 1-9
View Record in ScopusGoogle Scholar
[29]
B. Li, J. Quan, A. Loh, J. Chai, Y. Chen, C. Tan, X. Ge, T.S.A. Hor, Z. Liu, H. Zhang, Y. Zong
A robust hybrid Zn-battery with ultralong cycle life
Nano Lett., 17 (2017), pp. 156-163
View PDF
CrossRefView Record in ScopusGoogle Scholar
[30] Y. Ma, X. Xiao, W. Yu, W. Shang, P. Tan, Z. Wu, M. Ni

Mathematical modeling and numerical analysis of the discharge process of an alkaline zinc-cobalt battery
J. Energy Storage, 30 (2020), Article 101432
ArticleDownload PDFView Record in ScopusGoogle Scholar

[31] E. Deiss, F. Holzer, O. Haas
Modeling of an electrically rechargeable alkaline Zn-air battery
Electrochim. Acta, 47 (2002), pp. 3995-4010
ArticleDownload PDFView Record in ScopusGoogle Scholar

[32] K. Wang, J. Yu
Lifetime simulation of rechargeable zinc-air battery based on electrode aging
J. Energy Storage, 28 (2020), Article 101191
ArticleDownload PDFView Record in ScopusGoogle Scholar

[33] M. Venkatraman, J.W. Van Zee
A model for the silver-zinc battery during high rates of discharge
J. Power Sources, 166 (2007), pp. 537-548
ArticleDownload PDFView Record in ScopusGoogle Scholar

[34] E.U. Ubong, Z. Shi, X. Wang
Three-dimensional modeling and experimental study of a high temperature PBI-based PEM fuel cell
J. Electrochem. Soc., 156 (2009), pp. B1276-B1282
View PDF
CrossRefView Record in ScopusGoogle Scholar

[35] S. Um, C.-Y. Wang, K.S. Chen
Computational fluid dynamics modeling of proton exchange membrane fuel cells
J. Electrochem. Soc., 147 (2002), pp. 4485-4493
Google Scholar

[36] F Torabi, A. Aliakbar
A single-domain formulation for modeling and simulation of zinc-silver oxide batteries
J. Electrochem. Soc., 159 (2012), pp. A1986-A1992
View PDF
CrossRefGoogle Scholar

[37] L. Xiao, J. Lu, P. Liu, L. Zhuang
Determination of ionic conductivity and its impact on proton diffusion model for nickel hydroxide
J. Phys. Chem. B, 110 (2006), pp. 2057-2063
View PDF
CrossRefView Record in ScopusGoogle Scholar

[38] Z. Chen, W. Yu, Y. Liu, Y. Zeng, Q. He, P. Tan, M. Ni
Mathematical modeling and numerical analysis of alkaline zinc-iron flow batteries for energy storage applications
Chem. Eng. J., 405 (2020), Article 126684
Google Scholar

[39] R.M. Darling, J.P. Meyers
Mathematical model of platinum movement in PEM fuel cells
J. Electrochem. Soc., 152 (2005), pp. A242-A247

View PDF
CrossRefView Record in ScopusGoogle Scholar
[40]
X. Wang, F. Wang, L. Wang, M. Li, Y. Wang, B. Chen, Y. Zhu, L. Fu, L. Zha, L. Zhang, Y. Wu, W. Huang
An aqueous rechargeable Zn//Co_3O_4 battery with high energy density and good cycling behavior
Adv. Mater., 28 (2016), pp. 4904-4911
View PDF
CrossRefView Record in ScopusGoogle Scholar
[41] P. Tan, B. Chen, H. Xu, W. Cai, W. He, M. Ni
In-situ growth of Co_3O_4 nanowire-assembled clusters on nickel foam for aqueous rechargeable Zn-Co_3O_4 and Zn-air batteries
Appl. Catal. B Environ., 241 (2019), pp. 104-112
ArticleDownload PDFView Record in ScopusGoogle Scholar
[42] Y. Wang, Y. Zou, L. Tao, Y. Wang, G. Huang, S. Du, S. Wang
Rational design of three-phase interfaces for electrocatalysis
Nano Res., 12 (2019), pp. 2055-2066
View PDF
CrossRefView Record in ScopusGoogle Scholar
[43] C.H. Bartholomew
Mechanisms of catalyst deactivation
Appl. Catal. A Gen., 212 (2001), pp. 17-60
ArticleDownload PDFGoogle Scholar
[44] J.A. Moulijn, A.E. van Diepen, F. Kapteijn
Catalyst deactivation: is it predictable? What to do?
Appl. Catal. A Gen., 212 (2001), pp. 3-16
ArticleDownload PDFGoogle Scholar
[45] L. Zhang, X. Qin, S. Zhao, A. Wang, J. Luo, Z.L. Wang, F. Kang, Z. Lin, B. Li
Advanced matrixes for binder-free nanostructured electrodes in lithium-ion batteries
Adv. Mater., 32 (2020), Article 1908445
View PDF
CrossRefGoogle Scholar
[46] T. Jin, Q. Han, L. Jiao
Binder-free electrodes for advanced sodium-ion batteries
Adv. Mater., 32 (2020), pp. 1-14
Google Scholar

[47] Z. Xing, Y.-P. Deng, S. Sy, G. Tan, A. Li, J. Li, Y. Niu, N. Li, D. Su, J. Lu, Z. Chen

Carbon-pore-sheathed cobalt nanoseeds: An exceptional and durable bifunctional catalyst for zinc-air batteries
Nano Energy, 65 (2019), Article 104051
ArticleDownload PDFView Record in ScopusGoogle Scholar

[48]
R. Sakai, K. Murakami, Y. Mizutani, Y. Tanaka, S. Hayashi, A. Ishikawa, T. Higo, S. Ogo, H. T suneki, H. Nakai, Y. Sekine

Agglomeration suppression of a Fe-supported catalyst and its utilization for low-temperature ammonia synthesis in an electric field
ACS Omega, 5 (2020), pp. 6846-6851
View PDF
CrossRefView Record in ScopusGoogle Scholar

[49] T. Zhang, S. Zhang, S. Cao, Q. Yao, J.Y. Lee

Bridging the energy efficiency gap between quasi-neutral and alkaline rechargeable zinc-air batteries by an efficient hybrid battery design
Energy Storage Mater., 33 (2020), pp. 181-187
ArticleDownload PDFGoogle Scholar